ACS SENSORS

pubs.acs.org/acssensors

Article

Bidimensional Engineered Amorphous *a*-SnO_2 Interfaces: Synthesis and Gas Sensing Response to H_2S and Humidity

Valentina Paolucci,* Jessica De Santis, Vittorio Ricci, Luca Lozzi, Giacomo Giorgi,* and Carlo Cantalini

Cite This: *ACS Sens.* 2022, 7, 2058−2068

Read Online

ACCESS | Metrics & More | Article Recommendations | Supporting Information

ABSTRACT: Two-dimensional (2D) transition metal dichalcogenides (TMDs) and metal chalcogenides (MCs), despite their excellent gas sensing properties, are subjected to spontaneous oxidation in ambient air, negatively affecting the sensor's signal reproducibility in the long run. Taking advantage of spontaneous oxidation, we synthesized fully amorphous *a*-SnO_2 2D flakes (≈30 nm thick) by annealing in air 2D $SnSe_2$ for two weeks at temperatures below the crystallization temperature of SnO_2 (T < 280 °C). These engineered *a*-SnO_2 interfaces, preserving all the precursor's 2D surface-to-volume features, are stable in dry/wet air up to 250 °C, with excellent baseline and sensor's signal reproducibility to H_2S (400 ppb to 1.5 ppm) and humidity (10−80% relative humidity (RH)) at 100 °C for one year. Specifically, by combined density functional theory and ab initio molecular dynamics, we demonstrated that H_2S and H_2O compete by dissociative chemisorption over the same *a*-SnO_2 adsorption sites, disclosing the humidity cross-response to H_2S sensing. Tests confirmed that humidity decreases the baseline resistance, hampers the H_2S sensor's signal (i.e., relative response (RR) = R_a/R_g), and increases the limit of detection (LOD). At 1 ppm, the H_2S sensor's signal decreases from an RR of 2.4 ± 0.1 at 0% RH to 1.9 ± 0.1 at 80% RH, while the LOD increases from 210 to 380 ppb. Utilizing a suitable thermal treatment, here, we report an amorphization procedure that can be easily extended to a large variety of TMDs and MCs, opening extraordinary applications for 2D layered amorphous metal oxide gas sensors.

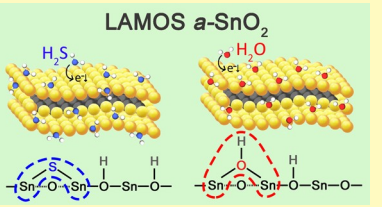

KEYWORDS: *$SnSe_2$, thermal oxidation, amorphous SnO_2, H_2S, water vapor, cross-influence, DFT, mechanism*

Two-dimensional (2D) layered transition metal dichalcogenide (TMD) and metal chalcogenide (MC) semiconductors, with near atomic-scale thickness, have been extensively proposed in the past decade as alternative materials for traditional nanocrystalline metal oxides (MO) for gas sensing applications.[1−4] Key advantages of these interfaces are represented by their high surface-to-volume ratios,[5] the direct-to-indirect band gap transition,[6,7] the occurrence of chemical terminations like edges, boundaries, and surface vacancies,[8−10] and the engineered functionalities by metal nanoparticle decoration or substitutional doping.[11,12] Despite these features, a substantial disadvantage of TMDs and MCs, adversely affecting sensors' signal reproducibility, is represented by their intrinsic thermodynamic instability (ΔG < 0), leading to spontaneous oxidation in dry-/wet-air laboratory conditions.[13,14] In details, the displacement of sulfur, selenium, and tellurium atoms, operated by ambient O_2 in MoS_2 and WS_2 sulfides,[15,16] $MoSe_2$, WSe_2, InSe, GaSe, and $SnSe_2$ selenides,[17−20] and $MoTe_2$ and WTe_2[21,22] tellurides, stimulates the nucleation over step edges of amorphous oxidized states, which proceeds through basal planes, eventually passivating all the flake's surface. This phenomenon is further enhanced when the sensor's operating temperature (OT) is increased in the range of 25−150 °C to compensate for irreversible adsorption of gas molecules, as frequently experienced in metal oxide and 2D layered sensors.[23,24]

Spontaneous oxidation of chalcogenides represents, indeed, an excellent opportunity to synthesize new kinds of interfaces comprising thin layers of amorphous metal oxides grown over 2D layered crystalline materials, yielding *a*-MO/TMD and *a*-MO/MC heterostructures with unexpected applications in the field of catalysis and gas sensing.[25] On this account, we recently demonstrated by means of experiments and theory that it is possible to synthesize *a*-SnO_2/$SnSe_2$ heterostructures to detect NO_2, H_2, NH_3, and humidity[26,27] by controlled oxidation in air of 2D exfoliated $SnSe_2$ layers. Besides their excellent gas sensing response, these 2D amorphous/2D crystalline heterostructures unfortunately retain some remarkable limitations. The difficulty of controlling the final thickness of the growing *a*-SnO_2 oxide over the 2D crystalline platform and the risk that the *a*-SnO_2 film is not self-passivating, i.e., not protecting the underlying 2D layer from further oxidation, make their practical exploitation challenging.[28]

Departing from liquid-phase exfoliated $SnSe_2$ layers (10−30 nm thick) and controlling the oxidation in air at 250 °C for two weeks, at temperatures below the crystallization temperature of *a*-SnO_2 oxide (i.e., ≈280 °C), we show for the first time that the oxidation process of 2D $SnSe_2$ can be successfully

Received: April 23, 2022
Accepted: June 13, 2022
Published: June 25, 2022

driven to the "core" of the flakes, yielding single-phase, fully amorphous 2D *a*-SnO_2, which is stable up to 250 °C and sensitive to H_2S gas (400 ppb to 1.5 ppm) and to humid air (10−80% RH (relative humidity) (RH @ 25 °C)) at a 100 °C operating temperature. Layered amorphous metal oxide sensors (LAMOS) like *a*-SnO_2 can be easily manufactured in a thin-film form by standard spin-coating deposition techniques representing a new interface for chemoresistive gas sensing applications. The amorphization thermal oxidation process here validated can be extended to a large variety of TMDs and MCs, opening new opportunities for "LAMOS" interfaces with unexplored surface-science capabilities, probably well beyond gas sensing applications.

RESULTS AND DISCUSSION

Thermal stability of exfoliated $SnSe_2$ flakes has been preliminarily investigated by simultaneous thermogravimetric (TG) and differential thermal analysis (DTA) techniques in air and nitrogen atmospheres by heating as-exfoliated $SnSe_2$ at 5 °C/min, to maximize the gain of the TG signal, to 1050 °C as shown in Figure 1a,b. In the range of 200−600 °C (Figure 1a),

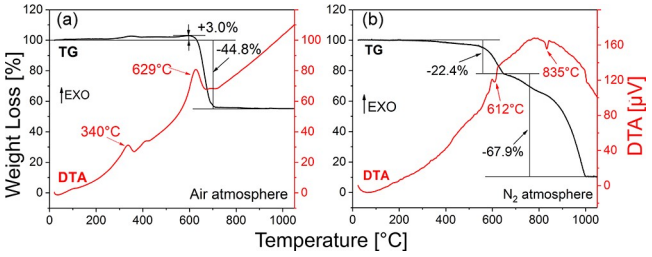

Figure 1. Thermogravimetric (TG) and differential thermal analysis (DTA) plots of as-exfoliated $SnSe_2$ flakes heated in air (a) and nitrogen (b) atmospheres at 5 °C/min from 25 to 1050 °C. Black and red lines refer to TG and DTA signals, respectively.

a weight increase of approximately 3.0% is recorded in static air corresponding to the onset of an exothermic peak of the DTA signal located at 340 °C. This result (i) is congruent with previous theoretical investigations predicting the formation of an intermediate $SnSe_2O_2$ oxide[26,29] and (ii) rules out any sublimation of SeO_2 species (eventually associated with a weight loss in Figure 1a), as previously found for $SnSe_2$ powders.[30] In the temperature range of 600−800 °C, the measured −44.8 ± 0.7% weight loss in air well agrees with the theoretical weight loss of −45.5% corresponding to the complete oxidation of $SnSe_2$ to SnO_2 (maximum rate at 629 °C).

Heating in a N_2 atmosphere in the 200−1000 °C range, as shown in Figure 1b, inhibits any weight gain, confirming the absence of substantial oxidation phenomena in a nitrogen atmosphere with increasing temperature. The measured weight losses in N_2 of −22.4% (at 612 °C) and −67.9% (at 835 °C) can be further attributed to the conversion of $SnSe_2$ to Sn_2Se_3[31,32] and the complete removal of Se and partial sublimation of Sn atoms, respectively,[31] as reported in the literature.

The surface chemical composition of annealed $SnSe_2$ at 250 °C for two weeks has been investigated by XPS analysis. Figure 2a−c shows the detailed XPS Sn 3d, O 1s (b), and Se 3d (c) core-level spectra of $SnSe_2$ flakes after two weeks of annealing in static air at 250 °C. Deconvolution of the Sn $3d_{5/2}$ core-level spectrum (Figure 2a) and quantitative analysis of the phases'

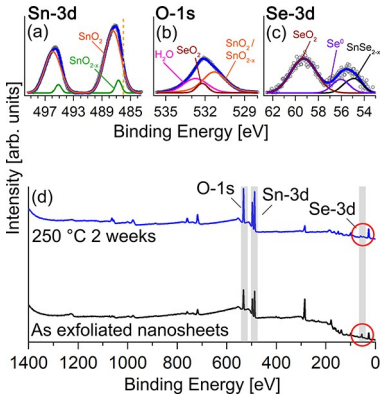

Figure 2. Deconvoluted Sn 3d (a), O 1s (b), and Se 3d (c) core-level spectra of $SnSe_2$ flakes after two weeks of annealing at 250 °C. Raw data (empty gray circles) and cumulative fits (blue lines) are reported. (d) Survey XPS spectra of $SnSe_2$ exfoliated nanosheets measured before (black) and after annealing (blue). Shaded gray areas highlight O 1s, Sn 3d, and Se 3d core levels.

composition shown in Table 1 highlight the complete oxidation of the surface, as demonstrated by the occurrence of two contributions ascribed to (i) stoichiometric SnO_2 (orange line) with maximum peak intensity of the $j = 5/2$ component centered at 487.4 eV[33] covering approximately 97% of the whole spectral area and (ii) defective SnO_{2-x} (green line) at 486.6 eV[34] representing nearly 3% of the entire signal.

The lack of any signal at 486.1 eV,[29,35] corresponding to the vertical dashed line of Figure 2a, confirms the absence of Sn−Se chemical bonds in the annealed sample. These results are congruent with O 1s and Se 3d core-level spectra of Figure 2b,c respectively. Specifically, the O 1s spectrum can be decomposed into three signals. The main peak, representing ≈50% of the total spectral area, is centered at 531.3 eV corresponding to Sn−O.[36−38] Those located at 532.2 and 532.7 eV are ascribed to SeO_2[39,40] (≈10%) and adsorbed H_2O[41] (≈40%), respectively. Finally, the Se 3d core-level spectrum (Figure 2c) comprises three contributions at 59.3, 56, and 54.6 eV, associated to SeO_2,[41] metallic Se,[42] and $SnSe_{2-x}$,[18] respectively.

According to Table 1, having set at 100% the cumulative spectral areas of Sn 3d, O 1s, and Se 3d, net of the elemental sensitivity of the XPS technique,[43] the relative atomic percentages of Se, Sn, and O yield Se 3d ≈ 3%, Sn 3d ≈ 18%, and O 1s ≈ 79%. In particular, the elemental ratio of O:Sn is found to be close to 2:1, which supports the occurrence of the SnO_2 phase.

Notably, the negligible contribution of the Se 3d signal in the annealed sample is confirmed in the survey spectra of Figure 2d exhibiting (compared by electronic magnification of the spectra in the red circles) the vanishing of the Se 3d signal in the annealed sample (blue line) with respect to the exfoliated $SnSe_2$ one (black line). It may be concluded that after controlled thermal treatment, the gas-responding surface of the annealed $SnSe_2$ flakes comprises almost stoichiometric SnO_2 and a negligible amount, approximately close to the instrumental resolution of the XPS equipment (±1%), of SeO_2 phases.

The amorphization process of $SnSe_2$ at different annealing times and temperatures has been investigated by the grazing incidence (GI)-XRD technique over spin-coated and annealed

https://doi.org/10.1021/acssensors.2c00887
ACS Sens. 2022, 7, 2058−2068

Table 1. Relative and Cumulative Surface Atomic Concentrations (at. %) of Sn, O, and Se Elements

					Sn $3d_{5/2}$		O 1s	Se $3d_{5/2}$
single spectral area [arbitrary units]					1417		6143	245
relative percentages (with respect to cumulative counts of Sn 3d, O 1s, and Se 3d)					18%		79%	3%
	SnO_2	SnO_{2-x}	H_2O	SeO_2	SnO_2	SeO_2	Se(0)	$SnSe_{2-x}$
BE [eV]	487.5	486.6	532.7	532.2	531.3	59.3	56	54.6
area [arbitrary units]	5961	168	1733	457	2148	109	29	36
relative %	97%	3%	40%	10%	50%	63%	17%	21%
cumulative %	18%	1%	31%	8%	38%	2%	1%	1%

thin films deposited over silicon substrates. According to Figure 3, as-exfoliated $SnSe_2$ exhibits a major diffraction peak

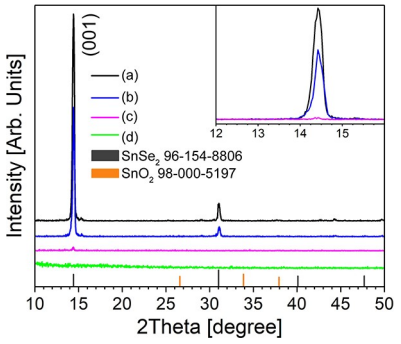

Figure 3. Grazing incidence (GI)-XRD diffraction patterns of as-exfoliated $SnSe_2$ flakes (a) and $SnSe_2$ annealed at 250 °C for one week (b), 250 °C for two weeks (c), and 250 °C for two weeks + one extra week at 280 °C (d).

(black line) corresponding to the (001) plane of $SnSe_2$ at $2\theta = 14.4°$ (ICDD card no. 96-154-8806). At 250 °C, with proceeding the annealing time from one week (blue line) to two weeks (magenta line), the (001) peaks almost disappear (see also the inset of Figure 3), confirming the effectiveness of the amorphization process. The two-weeks annealed sample at 250 °C (magenta), further annealed for an extra week at 280 °C, retains its amorphous structure (green), highlighting no substantial recrystallization phenomena of amorphous *a*-SnO_2 into crystalline SnO_2 as it will be further discussed in the HRTEM characterization.

The microstructural evolution of $SnSe_2$ flakes annealed at different times/temperatures, over selected flake's regions (Figure S1), has been characterized by HRTEM microscopy and is shown in Figure 4. As-exfoliated $SnSe_2$ (Figure 4a) exhibits a fully crystalline structure (SAED1), corresponding to the inner region of the flakes, with an interplanar distance of 0.30 nm (Figure 4e), congruent with the (001) crystallographic plane of $SnSe_2$ determined by GI-XRD. Notably, an amorphous edge (SAED2), extending by approximately 8 nm inside the flake's terrace, is also detectable (Figure 4e), which is congruent with an oxidation process mechanism advancing from the outside to the inside of the flakes, as extensively reported for TMD and MD materials.[13,18] Despite our previous research demonstrating no significant edge oxidation phenomena of liquid-phase exfoliated $SnSe_2$,[28] in this case, we attribute the step-edge amorphization process of $SnSe_2$ to the combined action of different sonicating conditions and the use of a different solvent (here NMP). With annealing at 250 °C for one week (Figure 4b,f), the degree of crystallization decreases compared to the as-exfoliated sample, as confirmed by the formation of halos in SAED patterns (i.e., compare SAED1 of Figure 4a with SAED2 of Figure 4b). The onset of an amorphization phenomenon is confirmed in Figure 4f where a patchwork of crystalline/amorphous phases is clearly displayed. With annealing for two weeks at 250 °C, crystalline domains of the parent $SnSe_2$ completely disappear, as exhibited in Figure 4c,g, confirming the completeness of the amorphization process. To conclude, we also tried to investigate the recrystallization mechanism of amorphous *a*-SnO_2 into crystalline SnO_2, as shown in Figure 4d,h. We found that by an extra week of annealing at 280 °C, crystalline domains are initially formed on step edges, as shown in Figure 4d with corresponding interatomic plane distances of 0.33 nm (Figure 4h), attributed to the (110) plane distances of tetragonal rutile SnO_2.[44] It turns out that the recrystallization of *a*-SnO_2 into crystalline SnO_2 proceeds from the outside to the inside of the flake, considering that no nucleating SnO_2 crystallites are

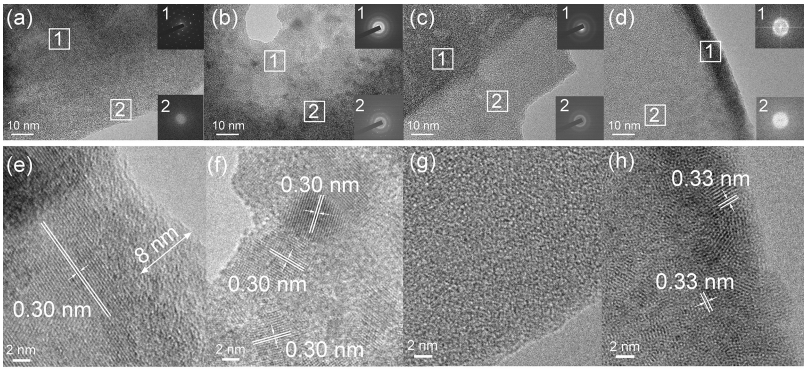

Figure 4. HRTEM pictures of (a,e) as-exfoliated $SnSe_2$ flakes and $SnSe_2$ (b,f) annealed at 250 °C for one week, (c,g) annealed at 250 °C for two weeks, and (d,h) annealed at 250 °C for two weeks + one extra week at 280 °C. SAED patterns corresponding to the identified regions are shown in the insets.

https://doi.org/10.1021/acssensors.2c00887
ACS Sens. 2022, 7, 2058−2068

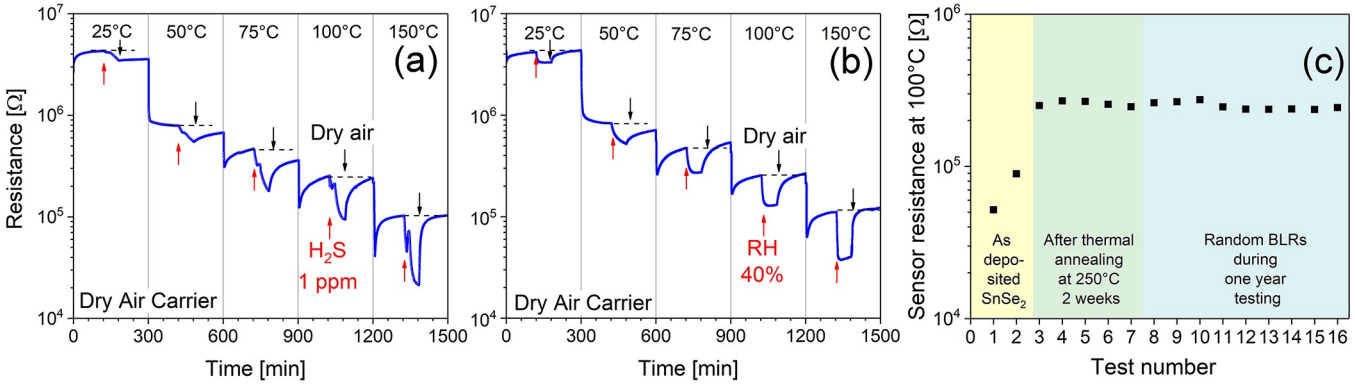

Figure 5. Electrical responses of the two-weeks/250 °C annealed *a*-SnO_2 sensor in dry air at different OTs (from 25 to 150 °C) to (a) 1 ppm H_2S and (b) 40% RH (RH @ 25 °C). (c) Baseline resistance evolution in dry air at a 100 °C OT of (i) as-exfoliated $SnSe_2$ (yellow region) and (ii) as-annealed (two weeks/250 °C) *a*-SnO_2 (green region) and (iii) *a*-SnO_2 thin-film baseline resistance randomly measured during one-year conditioning at 100 °C (blue region).

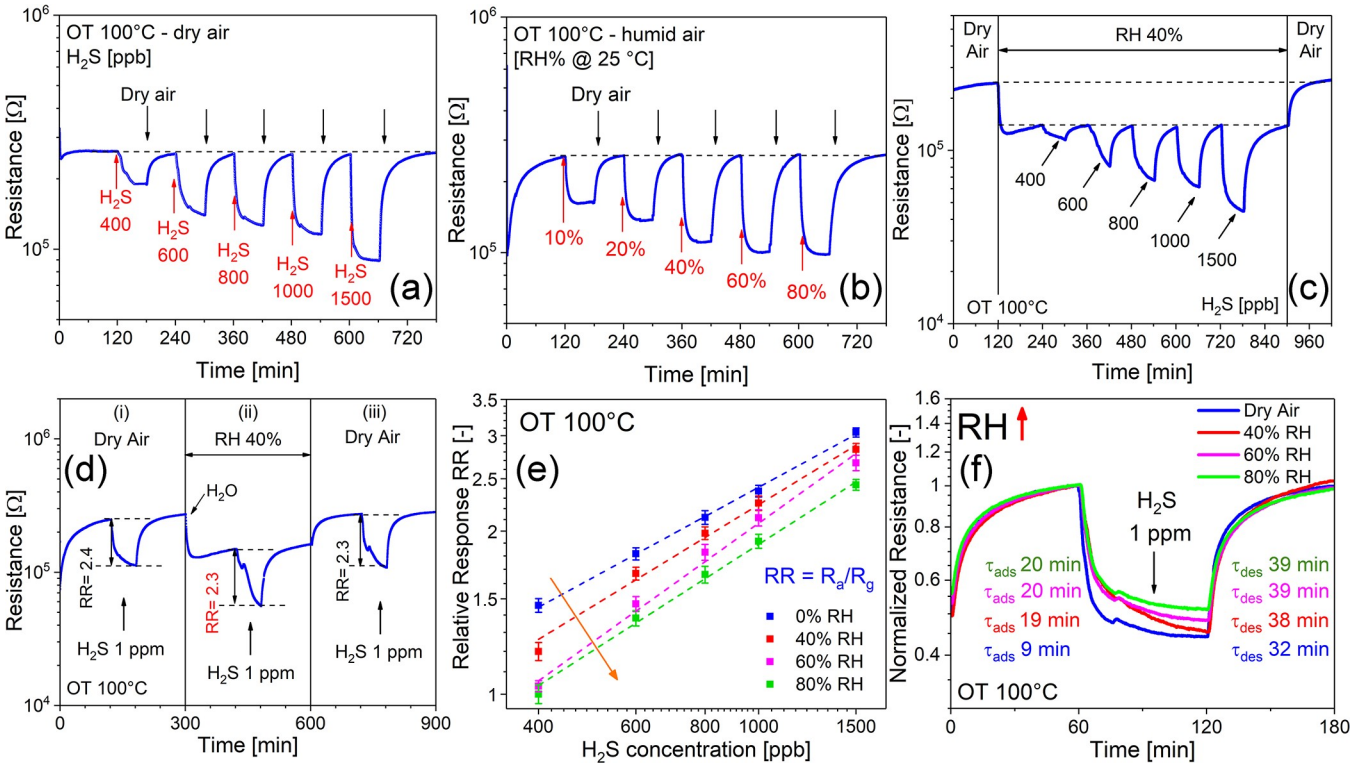

Figure 6. Dynamic electrical responses in dry air at a 100 °C OT to (a) H_2S (400 ppb to 1.5 ppm) and (b) H_2O in the range of 10−80% RH (RH @ 25 °C). (c) Dynamic electrical responses of *a*-SnO_2 at a 40% RH background and increasing concentrations of H_2S (400 ppb to 1.5 ppm). (d) 40% RH humidity cross-response to 1 ppm H_2S at a 100 °C OT: (i) first step in dry air and 1 ppm H_2S; (ii) second step at a 40% RH background and 1 ppm H_2S; (iii) third step, equivalent to (i), to check for short-term repeatability. (e) Log/log calibration plots at different RH values from 0 to 80% (as to the arrow) to increasing concentrations of H_2S, measured at a 100 °C OT (associated standard deviations calculated over a set of five consecutive measurements); (f) adsorption and desorption times of H_2S (1 ppm) to increasing RH values as to the red arrow.

visible inside the flakes as shown in Figure 4d,h. The limited extension of the crystalline domains with respect to the amorphous ones shown in Figure 4d,h may also explain the lack of any diffraction peak attributed to crystalline SnO_2 in the GI-XRD pattern of Figure 3.

In conclusion, the whole amorphization process here presented, comprising the recrystallization of *a*-SnO_2 to SnO_2, possibly represents interesting evidence of a nearly topotactic transformation of a 2D $SnSe_2$ metal chalcogenide into a 2D *a*-SnO_2 metal oxide, which includes loss of selenium and oxygen gain so that the final *a*-2D structure, retains the same bidimensional feature of the original material. This process represents a matter worthy of further investigation, eventually constituting a promising route to synthesize new metal oxide *a*-2D interfaces for gas sensing applications. Combining XPS, XRD, and HRTEM observations, it may be concluded that by annealing in air for two weeks at 250 °C, approximately 30 °C below the onset of the recrystallization temperature of *a*-SnO_2, the complete oxidation/amorphization of exfoliated 2D $SnSe_2$ flakes into 2D *a*-SnO_2 is achieved.

Gas Sensing Response to H_2S and Humidity. The best operating temperature (OT) for H_2S and H_2O of the two-

https://doi.org/10.1021/acssensors.2c00887
ACS Sens. 2022, 7, 2058−2068

weeks/250 °C annealed *a*-SnO_2 sample has been identified in light of two main features of the sensor's response: (i) sensor's signal amplitude, as represented by the relative response ratio (RR = R_{air}/R_{gas}), and (ii) recovery of the baseline resistance after gas desorption (BLR, i.e., the resistance in air at equilibrium). Tests have been carried out in the OT range of 25−150 °C in dry-air carrier gas exposing the film to 1 ppm H_2S and 40% relative humidity (40% @ 25 °C), as shown in Figure 5a,b respectively. By increasing the operating temperature, the sensor shows a monotonic decrease in the BLR, indicating a semiconducting behavior with an *n*-type response to both H_2S and humid-air reducing gases, consistent with preliminary results on *a*-SnO_2/$SnSe_2$ interfaces[28] and metal oxide SnO_2 sensors.[45]

According to Figure 5a, in the temperature range of 25−75 °C, the sensor displays a low signal response to 1 ppm H_2S and no recovery of the BLR (dashed black lines in the figure) even after 2 h of dry-air purge. With increasing the OTs, both the sensor's signal and desorption kinetics improve. The BLR is fully recovered, departing from the 100 °C OT, topping the best sensor's signal response at 150 °C. Poor recovery of the BLR in the temperature range of 25−75 °C, shown in Figure 5a, is a typical feature of a large variety of 2D TMD/MC gas sensor interfaces operated at near-room temperatures.[46] On this account, to improve gas desorption rates and BLR recovery, UV−vis light irradiation or increasing the sensor's operating temperature in the 75−150 °C range has been proposed for both traditional metal oxide[47,48] and 2D TMD/MD sensors.[49,50] These strategies indeed show remarkable limitations. UV-light irradiation of 2D TMDs/MDs requires almost monolayer thin interfaces (i.e., <5−7 nm),[46,51,52] whereas thermal heating at higher temperatures stimulates fast surface oxidation, hampering BLR reproducibility over the long run. On this account, *a*-SnO_2 annealed at 250 °C can be safely operated in the temperature range of 100−150 °C without any risk of further degradation or recrystallization, providing an effective solution for fast BLR recovery and improved sensor's signal reproducibility. Water vapor at 40% RH (RH @ 25 °C) behaves like H_2S, as shown in Figure 5b, with improved sensor's signal and BLR recovery in the temperature range of 100−150 °C (see also dynamic humidity responses in the range of 25−75 °C in Figure S4). Notably, a complete recovery of the baseline is also recorded at 25 °C, possibly on account of a protonic (H^+) Grotthuss chain-like conduction mechanism induced by physisorbed water at lower temperatures.[53] Departing from the 100 °C OT, most of the physisorbed water is removed[54] and water vapor responds as a reducing gas as previously reported.[55]

Baseline resistance reproducibility over the long run, under sustained OTs and dry/wet conditions, also represents a key issue for the exploitation of this new kind of interface. Figure 5c shows the evolution of the BLR in dry air recorded at a 100 °C OT of (i) as-exfoliated $SnSe_2$ (yellow region), (ii) two-weeks/250 °C annealed $SnSe_2$ (green region), and (iii) *a*-SnO_2 thin films after one-year conditioning at 100 °C (blue region). The amorphization process, producing truly stable *a*-SnO_2 oxide, sharply increases the BLR in dry air (yellow-green region), which finally stabilizes, exhibiting excellent reproducibility and stability (±5% of the BLR variation) over the long run (blue region). One-year recordings of the electrical resistance of *a*-SnO_2 to 1 ppm H_2S gas and 40% humidity, shown in Figure S5, confirmed a remarkable reproducibility with an associated uncertainty of the sensor's signal to H_2S gas and humidity as low as ±0.1 and ±0.2, respectively.

Figure 6a,b shows the dynamic resistance changes at a 100 °C OT of *a*-SnO_2 to H_2S (400 ppb to 1.5 ppm range) and H_2O (10−80% RH range, RH @ 25 °C) in dry-air carrier gas, respectively. Both H_2S and H_2O at a 100 °C OT yield strong interactions with the *a*-SnO_2 surface, indeed with excellent recovery of the BLR following each step of gas/humidity purge. The effect of the 40% RH background to the dynamic H_2S response shown in Figure 6c (see also Figure S6 at 60 and 80% RH backgrounds) highlights that humid water decreases the BLR, though preserving a satisfactory H_2S gas dynamic modulation.

The assessment of the sensor's signal variations when both humidity and H_2S compete at the same time over the sensor's surface represents another key issue of the sensor's performance. This feature, known as humidity cross-response (CR) to H_2S sensing, is shown in Figure 6d. The test comprises (i) a first step in dry air and 1 ppm H_2S, (ii) a second step at a 40% RH background and 1 ppm H_2S, and (iii) a third step, equivalent to (i), to check for short-term repeatability. Comparing the sensors' signals in dry (i) and wet conditions (ii), no relevant changes of the RRs (RR = R_a/R_g) are displayed, considering that 1 ppm H_2S yields an RR of 2.4 ± 0.1 in dry air and an RR of 2.3 ± 0.1 in humid air (40% RH), provided an associated sensor's signal uncertainty of ±0.1 (measured over a set of five consecutive measurements). Moreover, no substantial changes in the electrical response are displayed comparing panels (i) and (iii), demonstrating an excellent short-term repeatability.

The humidity cross-response (CR) to H_2S sensing in the whole gas/humidity concentration range at a 100 °C OT, as represented by the log−log calibration plots of the sensor's signal (i.e., RR = R_a/R_g) vs H_2S gas concentrations and different RH values, is shown in Figure 6e. Increasing relative humidity from dry conditions to 80% RH (as to the direction of the arrow), sensor's signal amplitude decreases. Specifically, at 1 ppm H_2S, sensor's signal amplitude decreases from an RR of 2.4 ± 0.1 at 0% RH to an RR of 1.9 ± 0.1 at 80% RH. Moreover, congruent with this tendency, water vapor has a negative effect on increasing the H_2S limit of detection (LOD). By numerical extrapolation of the calibration lines of Figure 6e (according to the methods in Supporting Information, Section S3), the theoretical LOD increases from 210 ppb at 0% RH to 380 ppb at 80% RH, confirming the inhibiting effect of water vapor upon H_2S sensing. The antisynergistic interaction of water vapor upon H_2S detection is also confirmed in Figure 6f and Figure S7, showing the adsorption/desorption times of 1 ppm H_2S as a function of the humidity content. Increasing RH % (as to the direction of the red arrow), the adsorption time of 1 ppm H_2S increases from 9 (@ 0% RH) to 20 min (@ 80% RH), while the sensors' signal amplitude decreases from an RR of 2.4 ± 0.1 at 0% RH to an RR of 1.9 ± 0.1 at 80% RH. As a concluding remark, the adsorption−desorption times here reported (order of minutes) are in most cases much longer than those frequently reported in the literature (order of seconds). On this account, it should be noted that response times are mostly dependent on the experimental conditions like the humidity content and gas fluid dynamics inside the test cell. As to the latter, the theoretical residence time of the gas (TRT) given by the ratio between the cell volume [cm^3] and the gas flow rate [cm^3/min] may significantly differ from the mean residence time (MRT), representing the actual time to

https://doi.org/10.1021/acssensors.2c00887
ACS Sens. 2022, 7, 2058−2068

completely fill/empty the test cell. In a previous paper utilizing NO_2 as a marker gas, we found that the characteristic MRT of our experimental setup is between 4 and 5 min[28] with respect to a TRT of only 1 min: Humidity as well influences response time. As shown in Figure 6f, the response time to 1 ppm H_2S almost doubles from dry to 80% RH wet conditions. In conclusion, when comparing response times of different sensors/gases, the experimental setup, the humidity content, and operating temperatures should always be considered and eventually normalized.

Gas sensing relative responses (RR = R_a/R_g) of selected sensors, calculated by normalizing literature data to 1 ppm H_2S in dry air and at different OTs, are compared in Table 2. In addition to traditional porous metal oxide sensors[56] and metal oxide heterostructures, which guarantee the most favorable catalytic efficiency, *a*-SnO_2 performs better than traditional 2D TMD/MD[1−4] sensors operated in the same temperature range (150−200 °C). 2D *n*-*n*/*p*-*n* heterostructures[1−4] operating at room temperature show RRs slightly smaller than that of *a*-SnO_2, excluding *n*-*n* $SnSe_2/SnO_2$[29] with an associated sensor's signal as high as 7.5 to 1 ppm H_2S gas. Regarding *n*-*n*/*p*-*n* 2D heterostructures, which can be classified as "decorated" interfaces since they almost comprise 3D crystalline metal oxide nanoparticles grown over 2D TMD/MD flakes, it is not usually appreciated that the naked 2D TMD/MD surfaces of the heterostructure, i.e., the ones not protected by the "decoration", are likely to be oxidized in dry/wet air in the long run, negatively affecting the reproducibility of the electrical signal.

Table 2. Comparison of the H_2S Gas Sensing Performances of Different Sensors' Interfaces Obtained by Normalizing Literature Data to 1 ppm H_2S in Dry Air

sensing materials	H_2S [ppm]	response R_a/R_g [−]	OT [°C]	ref.
3D metal oxide[56]				
SnO_2 porous NF	1	14.3	350	45
ZnO (thin film)	1	4.3	330	57
WO_3	1	4.5	330	58
CuO	1	1.8	135	59
p-Co_3O_4	1	2.0	210	60
3D metal oxide heterostructures				
MoO_3/SnO_2	1	9	115	61
Cu_2O/CuO	1	6.3	95	62
rGO/WO_3	1	7.7	330	58
ZnO/CuO	1	6.7	25	63
PdRh ZnO-HC	1	2.9	260	64
MoO_3/WO_3	1	14.0	250	65
2D transition metal dichalcogenides (TMDs) and metal chalcogenides (MCs)[1−4]				
p-type WS_2	1	1.1	200	66
n-type WS_2	1	1.2	150	67
$MoSe_2$	1	1.2	200	68
$SnSe_2$	1	1.8	200	29
2D *n*-*n*/*p*-*n* heterostructures[1,2,4]				
$SnO_2/SnSe_2$	1	7.5	25	29
CuO/MoS_2	1	1.1	25	69
Ag-$MoSe_2$/rGO	1	1.2	25	70
$SnSe_2/WO_3$	1	1.3	25	71
2D LAMOS (this work)				
a-SnO_2	1	2.4	100	this work

Theoretical Model of H_2S and Humidity Adsorption. To support the experimental results, we carried out DFT atomistic simulations of H_2S molecule adsorption utilizing the same theoretical model of water molecules anchoring on the amorphous *a*-$SnO_2/SnSe_2$ nanosheet (NS).[28,72,73] Three stable geometries, all chemisorbed, whose structure and energetics are shown in Figure 7 (1−3) and Table 3, respectively, are found according to the theoretical procedure described in the Supporting Information. Specifically, Figure 7 exhibits three configurations with broken H−S bonds (two O−H bonds are similarly formed), supporting previous findings over crystalline SnO_2 that molecularly adsorbed H_2S attack is not favored.[74] The first structure (**1**, see Figure 7, top) is characterized by a S atom bound both to one Sn (d_{Sn-S} = 2.47 Å) and to one O atom (d_{Sn-O} = 1.68 Å). This mechanism is exothermic by 1.38 eV (following eq S1 in the SI). Bader analysis confirms what is expected on the presence of a newly formed S−O bond, that is, a slightly positively charged sulfur atom (+0.19) because of the larger electronegativity of oxygen.

The second structure (**2** in Figure 7, middle) is the most thermodynamically stable (E_{ads} = −4.52 eV) and is

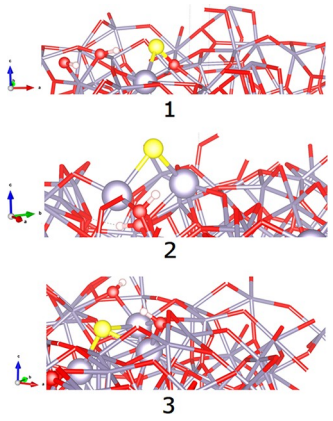

Figure 7. The three most stable optimized structures of H_2S anchored on top of the *a*-SnO_2 as obtained by DFT calculations on top of AIMD-calculated trajectories (see Computational Methods in Supporting Information, Section S4 for details) (yellow, S; mauve, Sn; red, oxygen; white, H atoms).

Table 3. Main Structural and Thermodynamic Data of the Three Most Stable Anchoring Mechanisms[a]

			Bader charge [charge units]		
adsorbate	structure	E_{ads} [eV]	S	H(1)	H(2)
H_2S	**1**	−1.38 (−0.28)	+0.19	+0.58	+0.60
H_2S	**2**	−4.52 (−3.42)	−0.71	+0.60	+0.64
H_2S	**3**	−3.65 (−2.55)	−0.72	+0.60	+0.59
			O	H(1)	H(2)
H_2O	**C2**	−1.24 (−2.02)	−0.52	−0.09	+0.15

[a]See Figure 7, **1**−**3**. E_{ads} is in eV, and the Bader charge is in elementary charge units. E_{ads} are values obtained by combining AIMD +DFT approaches for E_{surf_H2S} and (in brackets) values obtained still by combining AIMD+DFT approaches for the calculation of both E_{surf_H2S} and E_{surf} terms in eq S1 in Supporting Information, Section S4, which is the same for **C2**, i.e., the most stable anchoring mechanism of H_2O as described in ref 28. A Bader charge of >0 indicates charge transfer from the adsorbed species to the *a*-SnO_2 surface. A Bader charge of <0 indicates electron charge transfer from the *a*-SnO_2 surface to the adsorbed species.

https://doi.org/10.1021/acssensors.2c00887
ACS Sens. 2022, 7, 2058−2068

characterized by a sulfur atom bound to two Sn atoms. Such two Sn−S bonds are 2.44 and 2.46 Å, respectively, showing that the enhanced stability may be correlated with the shorter Sn−S bond length. In this case, the Bader analysis reveals an enhanced electron localization on S (−0.71), a fingerprint of the more marked electronegativity of S (compared to that of Sn, i.e., 2.58 vs 1.96).[75] The last structure (**3** in Figure 7, bottom), where the S atom is three-fold coordinated with Sn atoms (d_{Sn-S} = 2.46, 2.55, and 2.94 Å), is still markedly stabilized, compared to the reactants, with an adsorption energy of −3.65 eV and charge distribution on S (−0.72) very close to that in **2**. Regarding the H(1) and H(2) hydrogen adsorption modes, deriving from the rupture of the H_2S molecule, the Bader charge associated to the formation of O−H bonds with the O atoms at the surface is similar for all the three structures with a positive sign confirming the direction of the charge transfer from the adsorbed species to the *a*-SnO_2 surface.

An overall schematization of the most stable H_2S adsorption configuration over the optimized initial clean *a*-SnO_2 surface shown on the right-hand side of Figure 8a confirms the

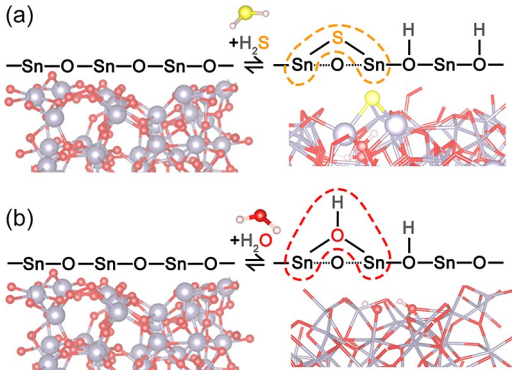

Figure 8. Schematization of the adsorption attack of H_2S and H_2O over the optimized clean *a*-SnO_2 surface. The left-hand side refers to the optimized initial clean *a*-SnO_2 system, and the right-hand side refers to the adsorption modes of H_2S (a) and H_2O (b). Yellow, S; mauve, Sn; red, oxygen; white, H atoms.

occurrence of a homolytic dissociation of H_2S with the formation of a rooted S atom, two-fold coordinated with Sn lattice atoms indicated as $(S)_{2Sn}$, and two rooted hydroxyls group (i.e., $(OH)_O$).

In the same fashion, as shown in the right-hand side of Figure 8b following a heterolytic rupture of OH bonds in H_2O,[28] water vapor chemisorbs over the *a*-SnO_2 surface with the formation of a rooted hydroxyl, two-fold coordinated with surface Sn atoms indicated as $(OH)_{2Sn}$, and one rooted hydroxyl group $(OH)_O$. Corresponding energetics and Bader charges are shown in the last line of Table 3, referring to the most stable H_2O attack (specifically **C2** in ref 28).

Gas Sensing Mechanism. At a 100 °C operating temperature, the adsorption of H_2S gas and H_2O over *a*-SnO_2 is experimentally transduced by a decrease in the sensor's resistance, as displayed in Figure 6a,b. In our case, we consider a clean *a*-SnO_2 amorphous surface where both H_2S and H_2O compete, as depicted in Figure 8a,b, at the same time over the same *a*-SnO_2 adsorption sites, according to the following reactions:

$$H_2S_{(g)} + 2Sn_{Sn} + 2O_O \rightleftarrows Sn_{Sn}^{n\delta^+} - S^{m\delta^-} - Sn_{Sn}^{n\delta^+} + 2(OH)_O \quad (1)$$

$$H_2O_{(g)} + 2Sn_{Sn} + O_O \rightleftarrows Sn_{Sn}^{n\delta^+} - OH^{m\delta^-} - Sn_{Sn}^{n\delta^+} + (OH)_O \quad (2)$$

$$(OH)_O \rightleftarrows (OH)_O^+ + e' \quad (3)$$

Compliant to theoretical computations, the positive (+) overall Bader charge balance of H_2S adsorption (see structure **2**, Table 3), derived from the balance of $n\delta^+$, $m\delta^-$, and hydroxyl−hydrogen atomic charge distribution as schematized by reaction 1, provides an electron enrichment of the *a*-SnO_2 surface, which is congruent to the decrease in the sensor's resistance with H_2S gas as shown in Figure 6a. Conversely, according to reaction 2, the negative (−) overall Bader charge balance of H_2O adsorption (see structure **C2**, Table 3[28]) confirms the electron depletion of the surface, which conflicts with the decrease in the sensor's resistance recorded in Figure 6b. This apparent contradiction can be explained accounting for the lower electron affinity of the rooted hydroxyls $(OH)_O$,which are easily ionized according to reaction 3, providing extra electrons (e′) that outweigh the negative charge depletion operated by water adsorption.

Fundamental investigations on the temperature interaction of water vapor over crystalline SnO_2 utilizing operando DRIFT spectroscopy[76] confirmed, opposite to our dissociative adsorption mechanism, that neither physisorption nor dissociative water adsorption occurs over the surface of crystalline SnO_2 in the temperature range of 100−150 °C. On this account, theoretical vs experimental conditions should always be considered. Our theoretical approach refers to a clean *a*-SnO_2 amorphous interface, while DRIFT experiments specifically apply to sol−gel-prepared crystalline SnO_2. Overall, it may be concluded that regardless of (i) the preparation conditions, (ii) the crystalline or amorphous nature of the interface, and (iii) the 2D or 3D geometry of the platform, in all cases, humidity substantially affects the resistance of the device. Specifically, it seems that the 2D layered nature of TMDs and MDs does not gain substantial advantages to improve humidity cross-interference compared to traditional metal oxide sensors. However, theoretical and practical investigations of the water vapor adsorption mechanism over 2D layered materials are still young, while effective practical strategies to promote selectivity have not been implemented yet.

It is our opinion that theoretical and experimental investigations at lower operating temperatures (OTs) are needed, considering that both metal oxide and 2D TMD/MD layered gas sensors are increasingly operated between room temperature and a 100 °C OT. On this account, the amorphous seamless texture of the *a*-SnO_2 sensor represents an ideal platform for operando DRIFT spectroscopy measurements considering the absence of crystalline planes, an opportunity that rules out any influence of the preparation conditions on the adsorption mechanism of different molecules.[77]

Figure 9 finally illustrates a possible effect of gas/water adsorption over layered *a*-SnO_2 and the conduction mechanism of nanosheet networks. Departing from few-layer gray-colored *a*-SnO_2 flakes, representing the situation in dry air

https://doi.org/10.1021/acssensors.2c00887
ACS Sens. 2022, 7, 2058−2068

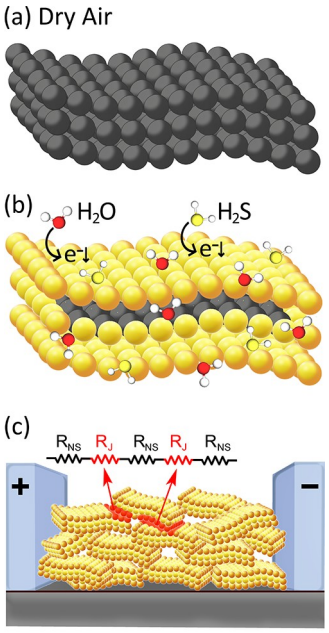

Figure 9. Schematization of a possible gas/water vapor adsorption mechanism over few flakes *a*-SnO_2 and the conduction mechanism of nanosheet networks. (a) Few-layer *a*-SnO_2 in dry air; (b) few-layer *a*-SnO_2 after exposure to H_2S or H_2O (yellow regions represent the charge injected zones and the gray inner regions the not injected ones); (c) network morphology of spin-coated *a*-SnO_2 flakes forming localized intersheet junctions (colored in red) with the schematization of the current transfer equivalent circuit between the sheets (R_{NS} = sheet resistance and R_J = junction resistance).

(Figure 9a), as soon as H_2S gas or H_2O adsorbs over *a*-SnO_2, the flake's surface charge carrier concentration increases, corresponding to the yellow-colored regions of Figure 9b. Depending on the thickness of the stacked flakes, the extension of the injected regions may be limited to surface layers, leaving the inner flakes unaffected (inner gray region of Figure 9b), or eventually extended to the core (fully injected flakes, not shown here). Remarkably, by controlling the liquid-phase exfoliation procedure,[78] the thickness of the flakes can be easily tailored to cover all the possible conduction regimes, from few-nanometer fully injected thin layers to partially injected thicker ones, therefore effectively modulating the gas response. Lastly, we have reported in Figure 9c the schematization of a spin-coated thin film, comprising a disordered network of *a*-SnO_2 nanosheets, forming localized intersheet junctions (highlighted in red in Figure 9c), and enabling charge transfer across the layers. In this case, the electrical conduction model is represented as an arrangement of in-series pairs of resistances where R_S and R_J represent the sheet and junction resistances, respectively, as recently brilliantly discussed.[79] Considering that amorphous oxide semiconductors are generally characterized by a high electron mobility (≈10 $cm^2/(V\ s)$)[80] exceptionally topping the field-effect mobility of ≈100 $cm^2/(V\ s)$ for amorphous SnO_2,[81] a junction-limited conduction mechanism where $R_J \gg R_S$ prevails. This model addresses the formation of Schottky barriers between the flakes, modulated by the nature and composition of the adsorbing gas in the same way as the conduction mechanism of loosely sintered metal oxide nanoparticles in traditional chemoresistive sensors.

CONCLUSIONS

We have reported an innovative and simple procedure to synthesize "LAMOS", specifically layered amorphous *a*-SnO_2 metal oxide sensors, by annealing liquid-phase exfoliated 2D $SnSe_2$ in air for two weeks at 250 °C. The oxidation process of 2D $SnSe_2$ here validated, carried out at temperatures below the crystallization temperature of SnO_2 (280 °C), enables the spontaneous substitution of sulfur with oxygen atoms in 2D $SnSe_2$. Such layered amorphous *a*-SnO_2 flakes, which are stable up to 250 °C, preserve all the geometrical features of their 2D precursor counterparts. Thin-film sensors of amorphous *a*-SnO_2 flakes, fabricated by spin-coating over patterned electrodes, are sensitive to H_2S and humidity at a 100 °C operating temperature, with excellent baseline resistance recovery and sensor's signal reproducibility over one-year deployment. We also found that the electrical response to H_2S and humidity of *a*-SnO_2 is like that of crystalline SnO_2 microporous metal oxides, with associated humidity cross-effects on H_2S sensing and a reduced sensor's signal amplitude with increasing the humidity content. We also demonstrated the hindering effect of water vapor upon H_2S sensing by a combined DFT+AIMD computational approach, highlighting that both H_2O and H_2S compete at the same time, over the same *a*-SnO_2 adsorption site, according to a dissociative chemisorption mechanism. We additionally indicated a possible conduction mechanism of the *a*-SnO_2 thin-film device, theorizing the formation of Schottky barriers between the flakes, modulated by the nature and composition of the adsorbing gas, in the same way as the conduction mechanism of loosely sintered metal oxide nanoparticles in traditional chemoresistive sensors.

In conclusion, we have validated an effective strategy to offset typical drift electrical signal phenomena in 2D TMD/MD sensors induced by spontaneous degradation in dry/wet ambient conditions of the sensor's surface. On this account, we validated a "core" oxidation/amorphization synthesis of pristine 2D $SnSe_2$ chalcogenide flakes to yield *a*-SnO_2 gas sensors. Remarkably, this methodology can be extended to a large variety of TMDs and MCs, opening new opportunities for "LAMOS" interfaces with unexplored surface-science capabilities, probably well beyond gas sensing applications.

ASSOCIATED CONTENT

Supporting Information

The Supporting Information is available free of charge at https://pubs.acs.org/doi/10.1021/acssensors.2c00887.

(Section S1) Microstructure, (Section S2) gas sensing, (Section S3) calculation of the low detection limit (LDL) and calibration lines to assess sensitivity, (Section S4) computational methods, and (Section S5) experimental section (PDF)

AUTHOR INFORMATION

Corresponding Authors

Valentina Paolucci − *Department of Industrial and Information Engineering and Economics, University of L'Aquila and UdR INSTM of L'Aquila, I-67100 L'Aquila, Italy;* orcid.org/0000-0003-0641-7926; Email: valentina.paolucci2@univaq.it

Giacomo Giorgi − *Department of Civil & Environmental Engineering (DICA), Università degli Studi di Perugia, 06125 Perugia, Italy; CNR-SCITEC, 06123 Perugia, Italy;*

https://doi.org/10.1021/acssensors.2c00887
ACS Sens. 2022, 7, 2058−2068

orcid.org/0000-0003-4892-7908;
Email: giacomo.giorgi@unipg.it

Authors

Jessica De Santis − *Department of Industrial and Information Engineering and Economics, University of L'Aquila and UdR INSTM of L'Aquila, I-67100 L'Aquila, Italy*

Vittorio Ricci − *Department of Industrial and Information Engineering and Economics, University of L'Aquila and UdR INSTM of L'Aquila, I-67100 L'Aquila, Italy*

Luca Lozzi − *Department of Physical and Chemical Sciences, University of L'Aquila, 67100 L'Aquila, Italy;* orcid.org/0000-0002-0150-5727

Carlo Cantalini − *Department of Industrial and Information Engineering and Economics, University of L'Aquila and UdR INSTM of L'Aquila, I-67100 L'Aquila, Italy*

Complete contact information is available at: https://pubs.acs.org/10.1021/acssensors.2c00887

Author Contributions

V.P. performed conceptualization, oversaw the research activity, conducted the research investigation process, evaluated the measurements, and wrote the original draft. J.D.S. performed materials characterization and developed a methodology for electrical characterization, preparation, and visualization of the published work. V.R. executed and validated the experiments. L.L. performed the research, investigations, and experiments. G.G. performed formal analysis by DFT+AIMD computational models to validate energetics and molecules' adsorption mechanisms and modeling of the amorphous structure of *a*-SnO_2. C.C. performed conceptualization, addressed the goals of the research, supervised and coordinated the experiments, and finalized the manuscript.

Notes

The authors declare no competing financial interest.

■ ACKNOWLEDGMENTS

TEM experiments at Jožef Stefan Institute-Ljubljana were carried out within the framework of the GAS-HYBRID-TMDS proposal within the ESTEEM3 (Enabling Science and Technology through European Electron Microscopy) project, which received funding from the European Union's Horizon 2020 Research and Innovation Programme under Grant Agreement No. 823717. G.G. acknowledges the availability of high-performance computing resources at Cineca under Iscra-B and Iscra-C initiatives. G.G. thanks the Dipartimento di Ingegneria Civile e Ambientale of the University of Perugia for allocating computing time within the project "Dipartimenti di Eccellenza 2018−2022".

■ REFERENCES

(1) Lee, E.; Yoon, Y. S.; Kim, D. J. Two-Dimensional Transition Metal Dichalcogenides and Metal Oxide Hybrids for Gas Sensing. *ACS Sens.* **2018**, *3*, 2045−2060.

(2) Kumar, R.; Goel, N.; Hojamberdiev, M.; Kumar, M. Transition Metal Dichalcogenides-Based Flexible Gas Sensors. *Sens. Actuators, A* **2020**, *303*, No. 111875.

(3) Tang, H.; Sacco, L. N.; Vollebregt, S.; Ye, H.; Fan, X.; Zhang, G. Recent Advances in 2D/Nanostructured Metal Sulfide-Based Gas Sensors: Mechanisms, Applications, and Perspectives. *J. Mater. Chem. A* **2020**, *8*, 24943−24976.

(4) Meng, Z.; Stolz, R. M.; Mendecki, L.; Mirica, K. A. Electrically-Transduced Chemical Sensors Based on Two-Dimensional Nanomaterials. *Chem. Rev.* **2019**, *119*, 478−598.

(5) Backes, C.; Campi, D.; Szydlowska, B. M.; Synnatschke, K.; Ojala, E.; Rashvand, F.; Harvey, A.; Griffin, A.; Sofer, Z.; Marzari, N.; Coleman, J. N.; O'Regan, D. D. Equipartition of Energy Defines the Size-Thickness Relationship in Liquid-Exfoliated Nanosheets. *ACS Nano* **2019**, *13*, 7050−7061.

(6) Gutiérrez, H. R.; Perea-López, N.; Elías, A. L.; Berkdemir, A.; Wang, B.; Lv, R.; López-Urías, F.; Crespi, V. H.; Terrones, H.; Terrones, M. Extraordinary Room-Temperature Photoluminescence in Triangular WS 2 Monolayers. *Nano Lett.* **2013**, *13*, 3447−3454.

(7) Huang, W.; Gan, L.; Li, H.; Ma, Y.; Zhai, T. 2D Layered Group IIIA Metal Chalcogenides: Synthesis, Properties and Applications in Electronics and Optoelectronics. *CrystEngComm* **2016**, *18*, 3968−3984.

(8) Nan, H.; Wang, Z.; Wang, W.; Liang, Z.; Lu, Y.; Chen, Q.; He, D.; Tan, P.; Miao, F.; Wang, X.; Wang, J.; Ni, Z. Strong Photoluminescence Enhancement of MoS2 through Defect Engineering and Oxygen Bonding. *ACS Nano* **2014**, *8*, 5738−5745.

(9) Agrawal, A. V.; Kumar, R.; Venkatesan, S.; Zakhidov, A.; Zhu, Z.; Bao, J.; Kumar, M. Fast Detection and Low Power Hydrogen Sensor Using Edge-Oriented Vertically Aligned 3-D Network of MoS2 Flakes at Room Temperature. *Appl. Phys. Lett.* **2017**, *111*, 093102.

(10) Agrawal, A. V.; Kumar, N.; Venkatesan, S.; Zakhidov, A.; Manspeaker, C.; Zhu, Z.; Robles Hernandez, F. C.; Bao, J.; Kumar, M. Controlled Growth of MoS2 Flakes from In-Plane to Edge-Enriched 3D Network and Their Surface-Energy Studies. *ACS Appl. Nano Mater.* **2018**, *1*, 2356−2367.

(11) Hao, L.; Liu, Y.; Du, Y.; Chen, Z.; Han, Z.; Xu, Z.; Zhu, J. Highly Enhanced H2 Sensing Performance of Few-Layer MoS2/SiO2/Si Heterojunctions by Surface Decoration of Pd Nanoparticles. *Nanoscale Res. Lett.* **2017**, *12*, 1.

(12) Burman, D.; Raha, H.; Manna, B.; Pramanik, P.; Guha, P. K. Substitutional Doping of MoS2for Superior Gas-Sensing Applications: A Proof of Concept. *ACS Sens.* **2021**, *6*, 3398−3408.

(13) Li, Q.; Zhou, Q.; Shi, L.; Chen, Q.; Wang, J. Recent Advances in Oxidation and Degradation Mechanisms of Ultrathin 2D Materials under Ambient Conditions and Their Passivation Strategies. *J. Mater. Chem. A* **2019**, *7*, 4291−4312.

(14) Wang, X.; Sun, Y.; Liu, K. Chemical and Structural Stability of 2D Layered Materials. *2D Mater.* **2019**, *6*, 042001.

(15) Gao, J.; Li, B.; Tan, J.; Chow, P.; Lu, T. M.; Koratkar, N. Aging of Transition Metal Dichalcogenide Monolayers. *ACS Nano* **2016**, *10*, 2628−2635.

(16) Rong, Y.; He, K.; Pacios, M.; Robertson, A. W.; Bhaskaran, H.; Warner, J. H. Controlled Preferential Oxidation of Grain Boundaries in Monolayer Tungsten Disulfide for Direct Optical Imaging. *ACS Nano* **2015**, *9*, 3695−3703.

(17) Mirabelli, G.; McGeough, C.; Schmidt, M.; McCarthy, E. K.; Monaghan, S.; Povey, I. M.; McCarthy, M.; Gity, F.; Nagle, R.; Hughes, G.; Cafolla, A.; Hurley, P. K.; Duffy, R. Air Sensitivity of MoS2, MoSe2, MoTe2, HfS2, and HfSe2. *J. Appl. Phys.* **2016**, *120*, 125102.

(18) Park, J. H.; Vishwanath, S.; Wolf, S.; Zhang, K.; Kwak, I.; Edmonds, M.; Breeden, M.; Liu, X.; Dobrowolska, M.; Furdyna, J.; Robinson, J. A.; Xing, H. G.; Kummel, A. C. Selective Chemical Response of Transition Metal Dichalcogenides and Metal Dichalcogenides in Ambient Conditions. *ACS Appl. Mater. Interfaces* **2017**, *9*, 29255−29264.

(19) Shi, L.; Zhou, Q.; Zhao, Y.; Ouyang, Y.; Ling, C.; Li, Q.; Wang, J. Oxidation Mechanism and Protection Strategy of Ultrathin Indium Selenide: Insight from Theory. *J. Phys. Chem. Lett.* **2017**, *8*, 4368−4373.

(20) Boukhvalov, D. W.; Nappini, S.; Vorokhta, M.; Menteş, T. O.; Piliai, L.; Panahi, M.; Genuzio, F.; De Santis, J.; Kuo, C. N.; Lue, C. S.; Paolucci, V.; Locatelli, A.; Bondino, F.; Politano, A. Revisiting the Chemical Stability of Germanium Selenide (GeSe) and the Origin of Its Photocatalytic Efficiency. *Adv. Funct. Mater.* **2021**, *31*, 1−13.

(21) Zhu, H.; Wang, Q.; Cheng, L.; Addou, R.; Kim, J.; Kim, M. J.; Wallace, R. M. Defects and Surface Structural Stability of MoTe2 under Vacuum Annealing. *ACS Nano* **2017**, *11*, 11005−11014.
(22) Ye, F.; Lee, J.; Hu, J.; Mao, Z.; Wei, J.; Feng, P. X. L. Environmental Instability and Degradation of Single- and Few-Layer WTe2Nanosheets in Ambient Conditions. *Small* **2016**, *12*, 5802−5808.
(23) Donarelli, M.; Prezioso, S.; Perrozzi, F.; Bisti, F.; Nardone, M.; Giancaterini, L.; Cantalini, C.; Ottaviano, L. Response to NO2 and Other Gases of Resistive Chemically Exfoliated MoS2-Based Gas Sensors. *Sens. Actuators, B* **2015**, *207*, 602−613.
(24) Perrozzi, F.; Emamjomeh, S. M.; Paolucci, V.; Taglieri, G.; Ottaviano, L.; Cantalini, C. Thermal Stability of WS2 Flakes and Gas Sensing Properties of WS2/WO3 Composite to H2, NH3 and NO2. *Sens. Actuators, B* **2017**, *243*, 812−822.
(25) Boukhvalov, D. W.; Paolucci, V.; D'Olimpio, G.; Cantalini, C.; Politano, A. Chemical Reactions on Surfaces for Applications in Catalysis, Gas Sensing, Adsorption-Assisted Desalination and Li-Ion Batteries: Opportunities and Challenges for Surface Science. *Phys. Chem. Chem. Phys.* **2021**, *23*, 7541−7552.
(26) Paolucci, V.; D'Olimpio, G.; Kuo, C. N.; Lue, C. S.; Boukhvalov, D. W.; Cantalini, C.; Politano, A. Self-Assembled SnO2/SnSe2Heterostructures: A Suitable Platform for Ultrasensitive NO2and H2Sensing. *ACS Appl. Mater. Interfaces* **2020**, *12*, 34362−34369.
(27) D'olimpio, G.; Genuzio, F.; Menteş, T. O.; Paolucci, V.; Kuo, C. N.; Al Taleb, A.; Lue, C. S.; Torelli, P.; Fariás, D.; Locatelli, A.; Boukhvalov, D. W.; Cantalini, C.; Politano, A. Charge Redistribution Mechanisms in SnSe2Surfaces Exposed to Oxidative and Humid Environments and Their Related Influence on Chemical Sensing. *J. Phys. Chem. Lett.* **2020**, 9003−9011.
(28) Paolucci, V.; De Santis, J.; Lozzi, L.; Giorgi, G.; Cantalini, C. Layered Amorphous *a*-SnO2 Gas Sensors by Controlled Oxidation of 2D-SnSe2. *Sens. Actuators, B* **2022**, *350*, No. 130890.
(29) Wang, T.; Wang, Y.; Sun, Q.; Zheng, S.; Liu, L.; Li, J.; Hao, J. Boosted Interfacial Charge Transfer in SnO2/SnSe2heterostructures: Toward Ultrasensitive Room-Temperature H2S Detection. *Inorg. Chem. Front.* **2021**, *8*, 2068−2077.
(30) Li, X.; Liu, W.; Huang, B.; Liu, H.; Li, X. Layered SnSe2 Microflakes and SnSe2/SnO2 Heterojunctions for Low-Temperature Chemiresistive-Type Gas Sensing. *J. Mater. Chem. C* **2020**, *8*, 15804−15815.
(31) Yan, Y.; Guo, T.; Song, X.; Yu, Z.; Jiang, Y.; Xia, C. Cu(In,Ga)Se2 Thin Films Annealed with SnSe2 for Solar Cell Absorber Fabricated by Magnetron Sputtering. *Sol. Energy* **2017**, *155*, 601−607.
(32) Shimada, T.; Ohuchi, F. S.; Parkinson, B. A. Thermal Decomposition of SnS 2 and SnSe 2 : Novel Molecular-beam Epitaxy Sources for Sulfur and Selenium. *J. Vac. Sci. Technol., A* **1992**, *10*, 539−542.
(33) Süzer, Ş.; Voscoboinikov, T.; Hallam, K. R.; Allen, G. C. Electron Spectroscopic Investigation of Sn Coatings on Glasses. *Anal. Bioanal. Chem.* **1996**, *355*, 654−656.
(34) Choi, W.-K.; Jung, H.-J.; Koh, S.-K. Chemical Shifts and Optical Properties of Tin Oxide Films Grown by a Reactive Ion Assisted Deposition. *J. Vac. Sci. Technol., A* **1996**, *14*, 359−366.
(35) Xu, T.; Han, Y.; Lin, L.; Xu, J.; Fu, Q.; He, H.; Song, B.; Gai, Q.; Wang, X. Self-Power Position-Sensitive Detector with Fast Optical Relaxation Time and Large Position Sensitivity Basing on the Lateral Photovoltaic Effect in Tin Diselenide Films. *J. Alloys Compd.* **2019**, *790*, 941−946.
(36) Chen, H.; Pu, X.; Gu, M.; Zhu, J.; Cheng, L. Tailored Synthesis of SnO2@graphene Nanocomposites with Enhanced Photocatalytic Response. *Ceram. Int.* **2016**, *42*, 17717−17722.
(37) Di Giulio, M.; Serra, A.; Tepore, A.; Rella, R.; Siciliano, P.; Mirenghi, L. Influence of the Deposition Parameters on the Physical Properties of Tin Oxide Thin Films. *Mater. Sci. Forum* **1996**, *203*, 143−148.
(38) Badrinarayanan, S.; Mandale, A. B.; Gunjikar, V. G.; Sinha, A. P. B. Mechanism of High-Temperature Oxidation of Tin Selenide. *J. Mater. Sci.* **1986**, *21*, 3333−3338.
(39) Martensson, N.; Malmqvist, P.-A.; Svensson, S.; Basilier, E.; Pireaux, J.-J.; Gelius, U.; Siegbahn, K. Molecular and Solid Water - A Comparative ESCA Study— the Research Portal - University of Namur. *Nouv. J. Chim.* **1977**, *1*, 191−196.
(40) Idriss, H. On the Wrong Assignment of the XPS O1s Signal at 531−532 EV Attributed to Oxygen Vacancies in Photo- and Electro-Catalysts for Water Splitting and Other Materials Applications. *Surf. Sci.* **2021**, *712*, 2−7.
(41) Zheng, Q.; Cheng, X.; Li, H. Microwave Synthesis of High Activity FeSe2/C Catalyst toward Oxygen Reduction Reaction. *Catalysts* **2015**, *5*, 1079−1091.
(42) Mandale, A. B.; Badrinarayanan, S.; Date, S. K.; Sinha, A. P. B. Photoelectron-Spectroscopic Study of Nickel, Manganese and Cobalt Selenides. *J. Electron Spectrosc. Relat. Phenom.* **1984**, *33*, 61−72.
(43) Moulder, J. F.; Stickle, W. F.; Sobol, P. E.; Bomben, K. D. *Handbook of X-Ray Photoelectron Spectroscopy*; Perkin-Elmer Corporation, 1992.
(44) Vafaei, S.; Wolosz, A.; Ethridge, C.; Schnupf, U.; Hattori, N.; Sugiura, T.; Manseki, K. Elucidation of the Crystal Growth Characteristics of SnO2 Nanoaggregates Formed by Sequential Low-Temperature Sol-Gel Reaction and Freeze Drying. *Nanomaterials* **2021**, *11*, 1738.
(45) Phuoc, P. H.; Hung, C. M.; Van Toan, N.; Van Duy, N.; Hoa, N. D.; Van Hieu, N. One-Step Fabrication of SnO2 Porous Nanofiber Gas Sensors for Sub-Ppm H2S Detection. *Sens. Actuators, A* **2020**, *303*, 1−11.
(46) Late, D. J.; Huang, Y. K.; Liu, B.; Acharya, J.; Shirodkar, S. N.; Luo, J.; Yan, A.; Charles, D.; Waghmare, U. V.; Dravid, V. P.; Rao, C. N. R. Sensing Behavior of Atomically Thin-Layered MoS2 Transistors. *ACS Nano* **2013**, *7*, 4879−4891.
(47) Giancaterini, L.; Emamjomeh, S. M.; De Marcellis, A.; Palange, E.; Resmini, A.; Anselmi-Tamburini, U.; Cantalini, C. The Influence of Thermal and Visible Light Activation Modes on the NO2 Response of WO3 Nanofibers Prepared by Electrospinning. *Sens. Actuators, B* **2016**, *229*, 387−395.
(48) Paolucci, V.; De Santis, J.; Lozzi, L.; Rigon, M.; Martucci, A.; Cantalini, C. ZnO Thin Films Containing Aliovalent Ions for NO2 Gas Sensor Activated by Visible Light. *Ceram. Int.* **2021**, *47*, 25017−25028.
(49) Paolucci, V.; Emamjomeh, S. M.; Ottaviano, L.; Cantalini, C. Near Room Temperature Light-Activated Ws2-Decorated Rgo as No2 Gas Sensor. *Sensors* **2019**, *19*, 2617.
(50) Chen, X.; Hu, J.; Chen, P.; Yin, M.; Meng, F.; Zhang, Y. UV-Light-Assisted NO2 Gas Sensor Based on WS2/PbS Heterostructures with Full Recoverability and Reliable Anti-Humidity Ability. *Sens. Actuators, B* **2021**, *339*, No. 129902.
(51) Kumar, R.; Goel, N.; Kumar, M. UV-Activated MoS2 Based Fast and Reversible NO2 Sensor at Room Temperature. *ACS Sens.* **2017**, *2*, 1744−1752.
(52) Tabata, H.; Matsuyama, H.; Goto, T.; Kubo, O.; Katayama, M. Visible-Light-Activated Response Originating from Carrier-Mobility Modulation of NO2Gas Sensors Based on MoS2Monolayers. *ACS Nano* **2021**, *15*, 2542−2553.
(53) Chen, Z.; Lu, C. Humidity Sensors: A Review of Materials and Mechanisms. *Sens. Lett.* **2005**, *3*, 274−295.
(54) Thiel, P. A.; Madey, T. E. The Interaction of Water with Solid Surfaces: Fundamental Aspects. *Surf. Sci. Rep.* **1987**, *7*, 211−385.
(55) Barsan, N.; Weimar, U. D. O. Conduction Model of Metal Oxide Gas Sensors. *J. Electroceram.* **2001**, *7*, 143−167.
(56) Guo, Z.; Chen, G.; Zeng, G.; Liu, L.; Zhang, C. Metal Oxides and Metal Salt Nanostructures for Hydrogen Sulfide Sensing: Mechanism and Sensing Performance. *RSC Adv.* **2015**, *5*, 54793−54805.
(57) Zhao, G.; Xuan, J.; Liu, X.; Jia, F.; Sun, Y.; Sun, M.; Yin, G.; Liu, B. Low-Cost and High-Performance ZnO Nanoclusters Gas

https://doi.org/10.1021/acssensors.2c00887
ACS Sens. 2022, 7, 2058−2068

Sensor Based on New-Type FTO Electrode for the Low-Concentration H 2 S Gas Detection. *Nanomaterials* **2019**, *9*, 1−10.
(58) Shi, J.; Cheng, Z.; Gao, L.; Zhang, Y.; Xu, J.; Zhao, H. Facile Synthesis of Reduced Graphene Oxide/Hexagonal WO3 Nanosheets Composites with Enhanced H2S Sensing Properties. *Sens. Actuators, B* **2016**, *230*, 736−745.
(59) Chen, Y. J.; Meng, F. N.; Yu, H. L.; Zhu, C. L.; Wang, T. S.; Gao, P.; Ouyang, Q. Y. Sonochemical Synthesis and Ppb H2S Sensing Performances of CuO Nanobelts. *Sens. Actuators, B* **2013**, *176*, 15−21.
(60) Prikhodko, K.; Nasriddinov, A.; Vladimirova, S.; Rumyantseva, M.; Gaskov, A. Nanocrystalline Oxides Nix Co3−x O4: Sub-Ppm H2 s Sensing and Humidity Effect. *Chemosensors* **2021**, *9*, 1−14.
(61) Gao, X.; Ouyang, Q.; Zhu, C.; Zhang, X.; Chen, Y. Porous MoO3/SnO2 Nanoflakes with n-n Junctions for Sensing H2S. *ACS Appl. Nano Mater.* **2019**, *2*, 2418−2425.
(62) Meng, F. N.; Di, X. P.; Dong, H. W.; Zhang, Y.; Zhu, C. L.; Li, C.; Chen, Y. J. Ppb H2S Gas Sensing Characteristics of Cu2O/CuO Sub-Microspheres at Low-Temperature. *Sens. Actuators, B* **2013**, *182*, 197−204.
(63) Wang, H.; Luo, Y.; Liu, B.; Gao, L.; Duan, G. CuO Nanoparticle Loaded ZnO Hierarchical Heterostructure to Boost H2S Sensing with Fast Recovery. *Sens. Actuators, B* **2021**, *338*, No. 129806.
(64) Luo, N.; Chen, Y.; Zhang, D.; Guo, M.; Xue, Z.; Wang, X.; Cheng, Z.; Xu, J. High-Sensitive MEMS Hydrogen Sulfide Sensor Made from PdRh Bimetal Hollow Nanoframe Decorated Metal Oxides and Sensitization Mechanism Study. *ACS Appl. Mater. Interfaces* **2020**, *12*, 56203−56215.
(65) Hu, J.; Sun, Y.; Wang, X.; Chen, L.; Zhang, W.; Chen, Y. Synthesis and Gas Sensing Properties of Molybdenum Oxide Modified Tungsten Oxide Microstructures for Ppb-Level Hydrogen Sulphide Detection. *RSC Adv.* **2017**, *7*, 28542−28547.
(66) Asres, G. A.; Baldoví, J. J.; Dombovari, A.; Järvinen, T.; Lorite, G. S.; Mohl, M.; Shchukarev, A.; Pérez Paz, A.; Xian, L.; Mikkola, J. P.; Spetz, A. L.; Jantunen, H.; Rubio, Á.; Kordás, K. Ultrasensitive H2S Gas Sensors Based on P-Type WS2 Hybrid Materials. *Nano Res.* **2018**, *11*, 4215−4224.
(67) Alagh, A.; Annanouch, F. E.; Colomer, J. F.; Llobet, E. 3D Assembly of WS2nanomaterial for H2S Gas Sensing Application. *Proc. IEEE Sensors* **2020**, *2020-Octob*, 2020−2023.
(68) Jha, R. K.; D'Costa, J. V.; Sakhuja, N.; Bhat, N. MoSe2 Nanoflakes Based Chemiresistive Sensors for Ppb-Level Hydrogen Sulfide Gas Detection. *Sens. Actuators, B* **2019**, *297*, No. 126687.
(69) Zhang, D.; Wu, J.; Cao, Y. Ultrasensitive H2S Gas Detection at Room Temperature Based on Copper Oxide/Molybdenum Disulfide Nanocomposite with Synergistic Effect. *Sens. Actuators, B* **2019**, *287*, 346−355.
(70) Luo, Y.; Zhang, D.; Fan, X. Hydrothermal Fabrication of Ag-Decorated MoSe/Reduced Graphene Oxide Ternary Hybrid for HS Gas Sensing. *IEEE Sens. J.* **2020**, *20*, 13262−13268.
(71) Guo, X.; Ding, Y.; Liang, C.; Du, B.; Zhao, C.; Tan, Y.; Shi, Y.; Zhang, P.; Yang, X.; He, Y. Humidity-Activated H2S Sensor Based on SnSe2/WO3 Composite for Evaluating the Spoilage of Eggs at Room Temperature. *Sens. Actuators, B* **2022**, *357*, No. 131424.
(72) Manzhos, S.; Giorgi, G.; Yamashita, K. A Density Functional Tight Binding Study of Acetic Acid Adsorption on Crystalline and Amorphous Surfaces of Titania. *Molecules* **2015**, *20*, 3371−3388.
(73) Prasai, B.; Cai, B.; Underwood, M. K.; Lewis, J. P.; Drabold, D. A. Properties of Amorphous and Crystalline Titanium Dioxide from First Principles. *J. Mater. Sci. 2012 4721* **2012**, *47*, 7515−7521.
(74) Wei, W.; Dai, Y.; Huang, B. Role of Cu Doping in SnO2 Sensing Properties toward H 2S. *J. Phys. Chem. C* **2011**, *115*, 18597−18602.
(75) Pauling, L. *The Nature of the Chemical Bond*, 3rd ed.; Cornell University Press, 1960.
(76) Degler, D.; Junker, B.; Allmendinger, F.; Weimar, U.; Barsan, N. Investigations on the Temperature-Dependent Interaction of Water Vapor with Tin Dioxide and Its Implications on Gas Sensing. *ACS Sens.* **2020**, *5*, 3207−3216.
(77) Wicker, S.; Guiltat, M.; Weimar, U.; Hémeryck, A.; Barsan, N. Ambient Humidity Influence on CO Detection with SnO2 Gas Sensing Materials. A Combined DRIFTS/DFT Investigation. *J. Phys. Chem. C* **2017**, *121*, 25064−25073.
(78) Paolucci, V.; D'Olimpio, G.; Lozzi, L.; Mio, A. M.; Ottaviano, L.; Nardone, M.; Nicotra, G.; Le-Cornec, P.; Cantalini, C.; Politano, A. Sustainable Liquid-Phase Exfoliation of Layered Materials with Nontoxic Polarclean Solvent. *ACS Sustainable Chem. Eng.* **2020**, *8*, 18830−18840.
(79) Kelly, A. G.; O'Suilleabhain, D.; Gabbett, C.; Coleman, J. N. The Electrical Conductivity of Solution-Processed Nanosheet Networks. *Nat. Rev. Mater.* **2022**, 217.
(80) Nomura, K.; Ohta, H.; Takagi, A.; Kamiya, T.; Hirano, M.; Hosono, H. Room-Temperature Fabrication of Transparent Flexible Thin-Film Transistors Using Amorphous Oxide Semiconductors. *Nature* **2004**, *432*, 488−492.
(81) Avis, C.; Kim, Y. G.; Jang, J. Amorphous Tin Oxide Applied to Solution Processed Thin-Film Transistors. *Materials* **2019**, *12*, 3341.

https://doi.org/10.1021/acssensors.2c00887
ACS Sens. 2022, 7, 2058−2068